Structural Complexities in Sodium Ion Conductive Antiperovskite Revealed by Cryogenic Transmission Electron Microscopy

Blanka E. Janicek[1], Sunil Mair[2], Yet-Ming Chiang[2], Colin Ophus[3], and Xi Jiang[1*]

1. Materials Sciences Division, Lawrence Berkeley National Laboratory, Berkeley CA, 94720. USA
2. Department of Materials Science and Engineering, Massachusetts Institute of Technology, Cambridge, MA, 02139. USA
3. The National Center for Electron Microscopy, Molecular Foundry, Lawrence Berkeley National Laboratory, Berkeley CA, 94720. USA

*Corresponding author: xijiang@lbl.gov

Abstract:

We use low-dose cryogenic transmission electron microscopy (cryo-TEM) to investigate the atomic-scale structure of antiperovskite $Na_2NH_2BH_4$ crystals by preserving the room-temperature cubic phase and carefully monitoring the electron dose. Via quantitative analysis of electron beam damage using selected area electron diffraction, we find cryogenic imaging provides six-fold improvement in beam stability for this solid electrolyte. Cryo-TEM images obtained from flat crystals revealed the presence of a new, long-range-ordered supercell with a cubic phase. The supercell exhibits doubled unit cell dimensions of 9.4 Å x 9.4 Å as compared to the cubic lattice structure revealed by X-ray crystallography of 4.7 Å x 4.7 Å. The comparison between the experimental image and simulated potential map indicates the origin of the supercell is a vacancy ordering of sodium atoms. This work demonstrates the potential of using cryo-TEM imaging to study the atomic-scale structure of air- and electron-beam sensitive antiperovskite-type solid electrolytes.

Keywords: Antiperovskites; Solid electrolyte; Cryo-TEM; Atomic-scale; Beam damage; Superlattice.

Solid-state electrolytes, such as garnet-type oxides (e.g., $Li_7La_3Zr_2O_{12}$),[1] sulfides of the argyrodite-type (e.g., $Li_{10}GeP_2S_{12}$),[2] and oxides of the perovskite-type (e.g., $La_{0.5}Li_{0.5}TiO_3$),[3] have gained tremendous attention as a practical solution to address battery safety concerns, offering enhanced energy density and chemical stability compared to liquid electrolytes.[4,5] The antiperovskite-type solid electrolyte sodium amide borohydride ($Na_2NH_2BH_4$), which was initially synthesized as for hydrogen storage,[6] has recently attracted significant attention due to the presence of two distinct cluster ions (NH_2 and BH_4) and the compositional flexibility of structural design.[7-12] The cation transportation is theorized to be the result of a rotational mechanism of two anion clusters (known as the double Paddle-wheel mechanism) that enhances the movement of cations and lowers energy barriers for their diffusion and migration through disordered cation vacancies.[12] X-ray scattering and diffraction may not always capture local defects and inhomogeneities, which arise from intrinsic structural flexibility of $Na_2NH_2BH_4$. High-resolution electron microscopy imaging is critical for thoroughly understanding such local structural details, which are of great importance for the rational design of solid electrolytes.[13-20]

It has been observed that not all solid electrolytes are free of radiation-induced structural damage after the exposure to the electron beam.[20, 21] Cooling the samples to liquid nitrogen (LN_2) temperature in the electron column after the air-free transfer has significantly reduced beam damage in solid electrolytes during imaging, which led to the direct observation of local lattices, interfaces, and dynamic properties of solid electrolytes and electrodes at various length scales.[20, 22-31] Nevertheless, the conventional air-free transfer methods face challenges in addressing the combined challenge of air and electron beam sensitivity, and as a result direct atomic-resolution imaging of the $Na_2NH_2BH_4$ solid electrolyte has not yet been reported.

Recently, a combination of cryo-TEM and the cryogenic plunging method, inspired by imaging techniques used for beam-sensitive biomaterials and soft materials, has been developed to preserve the natural structures of electrolytes, solid electrolyte interfaces, and lattices in electrodes.[18,24,26,27,30] This approach enables direct visualization of well-preserved lattice structures at the atomic scale with minimal electron beam damage. While these approaches have been effective in preserving the inherent lattice structures of solid electrolytes for high-resolution cryo-TEM imaging, it should be noted that previous studies were constrained to materials that do not exhibit phase transitions under the ambient temperature.

In this study, a robust cryogenic transfer protocol used to preserve the natural structures of this air-sensitive solid electrolyte crystals is developed. Cryo-TEM is used to image the atomic structure of $Na_2NH_2BH_4$ crystals by minimizing electron beam damage and preserving the room-temperature cubic lattice. We quantitatively analyze the beam damage on the lattice structures by measuring the critical dose of Bragg spots in electron diffraction patterns obtained from bulk cubic crystals. Ultra-thin planar $Na_2NH_2BH_4$ crystals are imaged while minimizing electron beam damage. Surprisingly, the analysis of the micrographs shows a long-range ordered superlattice with a doubled unit cell size, 9.4 x 9.4 Å, compared to the previously measured cubic unit cell, 4.7 x 4.7 Å, from X-ray diffraction.[12, 32, 33] Our observations indicate a presence of a superlattice with double the unit cell dimensions of cubic lattice, which was not observed in previous studies. Comparative analysis of atomic models, experimental cryo-TEM images, and simulated TEM images suggests that the origin of the superlattice is ordering of vacant sodium sites. These findings demonstrate the rich structural information accessible through atomic-scale cryo-TEM imaging of cluster-ion antiperovskite crystals.

Figure 1A depicts the unit cell of the cubic phase of $Na_2NH_2BH_4$ crystal with the $Pm\bar{3}m$ symmetry, with a lattice parameter of 4.7 Å. The amide anion occupies the body center site, and borohydride anions occupy the corner sites. Sodium cations occupy the face center sites, with two vacant sites to maintain charge balance. The simulated diffraction pattern of the cubic lattice is shown in Figure 1B, where dashed circles indicate the reflections corresponding to the lattice parameter of 4.7 Å. This spacing aligns with the X-ray diffraction measurements reported in literature.[12, 32, 33]

$Na_2NH_2BH_4$ crystal undergoes a phase transformation from a cubic to an orthorhombic at a transition temperature of 288 K. Consequently, conventional air-free transfer at room temperature followed by cooling to LN2 temperature in the column results in the loss of the cubic phase. We employed a cryogenic plunging method to preserve the high-temperature cubic phase which is the phase of interest for solid electrolyte materials because it exhibits ion conductivity. The method involves rapidly plunging a sealed container containing the TEM grid with deposited crystals into liquid nitrogen to prevent the phase transition. It utilized a reusable container design, as illustrated in Figure 2A. TEM grids were dipped into powdered crystals and carefully positioned on the lower Kapton film. A rubber pad with a hole (approximately 3 mm) smaller than the TEM grid diameter was placed above the TEM grid to prevent contact between the crystals and the upper Kapton film. Two O-rings were used to seal the aluminum cell assembly, secured by four screws. Subsequently, the assembled cell was transferred out of the glove box and immediately plunged into liquid nitrogen, as depicted in Figure 2B. The enhanced thermal conductivity resulting from the close contact between the grid and the Kapton film contributes to a more efficient cooling rate, in contrast to comparable methods employing plastic

tubes[27] or bags[29, 30, 34] as containers, which provide less surface area contact between the samples and the cryogen. The cell was disassembled under liquid nitrogen, and the grid was preserved and transferred into the microscope in liquid nitrogen to ensures the air-free structure is preserved. Figure 2C presents a cryo-TEM micrograph of the crystals prepared using this method. Figure 2D exhibits the corresponding diffraction pattern obtained from the crystal indicated in Figure 2C. The presence of sharp spots (up to 0.7 Å) indicates that the crystal was well-preserved using the combination of the air-tight cell and cryo-transfer method. More diffraction patterns obtained from bulk crystals are shown in Figure S1. Additionally, EDS mapping was conducted to investigate the oxygen distribution within the crystals. No obvious oxygen signals were observed from the interior region of crystals as shown in the EDS maps in Figure S2.

The electron beam sensitivity in antiperovskites varies based on their chemical composition and crystal structure. In the case of $Na_2NH_2BH_4$ crystals, the presence of all light elements and high vacancy content indicates a potential for higher beam sensitivity compared to conventional antiperovskites. Accordingly, the achievable resolution in a sample is constrained by beam damage.[21, 35] Therefore, it is crucial to investigate the durability of $Na_2NH_2BH_4$ under the electron beam before carrying out high-resolution cryo-TEM imaging.

Quantitative analysis of radiation damage in $Na_2NH_2BH_4$ crystals was conducted using selected area electron diffraction (SAED) at LN_2 temperature. A series of diffraction patterns were recorded from the same bulk crystal by applying an accumulated electron dose of 60 e/Å^2. The fading of reflections after reaching 60 e/Å^2 is demonstrated in a movie (Movie S1). Figure 3A shows the initial diffraction pattern obtained from a $Na_2NH_2BH_4$ crystal prepared using the

cryo-transfer method described in Figure 2 after electron beam exposure of approximately 3 e/Å^2. Four reflections at different spatial frequencies, ranging from 2.1 to 4.7 Å, are labeled with colored circles for quantitative measurement of the critical dose in Figure 3A. More high-order reflections are clearly visible. The dose-limited resolution is inversely proportional to the square root of the critical dose (*Dc*), representing the relative beam sensitivity, while the *Dc* is defined as the accumulated dose at which the intensity of a reflection (I) reduces to 37% of its initial intensity (I_0).[36, 37] The decreases in relative intensity at the four different diffraction spots (4.7 Å, 3.3 Å, 2.4 Å, and 2.1 Å) shown in Figure 3A are plotted in Figure 3B. Gaussian fitting of the spot amplitudes as a function of accumulated dose reveals an exponential decay for all measured spots. The critical dose is determined by the dose at which the intensity of the spot decreases to 37%, as indicated by dashed lines. The *Dc* decreases from 29 *e*/Å^2 at 4.7 Å to 17 *e*/Å^2 at 2.1 Å, suggesting that high spatial frequency signals, which represent the highly ordered lattice structures in $Na_2NH_2BH_4$ crystals, are more vulnerable to the electron beam.

The critical dose was also measured at room temperature for the comparison. The electron diffraction patterns acquired at room temperature were obtained using a conventional air-free transfer holder. Figure 3C presents the comparison at a high spatial frequency spot (2.1 Å). The critical doses are 17 *e*/Å^2 at 98 K and 2.7 *e*/Å^2 at 298 K for the 2.1 Å spot, indicating an approximately six-fold improvement in critical dose at the LN_2 temperature. These comparisons exhibit the importance of cryo-transfer and low-dose cryo-TEM imaging to preserve atomic-scale structures in $Na_2NH_2BH_4$ crystals which are comprised of highly hygroscopic amide compounds.

Critical dose measurements offer insights into the durability of crystals when exposed to an electron beam and inform usable dose limits that preserve the atomic-scale structure for cryo-TEM imaging. Nevertheless, achieving a high-resolution image of the pristine cubic lattice (4.7 Å) from bulk crystals in the micrometer size, which were used for electron diffraction, is challenging due to their thickness significantly exceeding the mean free path of 300 keV electrons. In addition to bulk crystals, smaller, flat crystals were observed adjacent to the bulk crystals (Figure S3). These flat crystals offer a potential for high-resolution imaging.

Low-dose cryo-TEM images obtained from the flat crystals with an accumulated dose of 22 $e/Å^2$ at LN_2 temperature reveal the crystal structure directly. Figure 4A displays a contrast transfer function (CTF)-corrected micrograph obtained from a flat $Na_2NH_2BH_4$ crystal (see Figure S4 for the other crystal). The presence of straight edges and the relatively low contrast, compared to the supporting carbon film, suggests that the crystal is likely a two-dimensional crystal. The white region along the perimeters represents the Fresnel fringe induced by defocus. Figure 4B illustrates the power spectrum of the image in Figure 4A, revealing strong reflections that indicate a well-ordered lattice in the crystal. The reflections were indexed to determine the lattice parameters, and only a portion of the power spectrum is shown for clarity of d-spacing. The full power spectrum and the fitting of CTF is shown in Figure S5. Surprisingly, the first-order lattice is observed at 9.4 Å (indicated by purple circles), double the dimensions of 4.7 Å as revealed by X-ray crystallography and the electron diffraction patterns obtained from bulk crystals (Figure 3).[12, 33] The indexing of reflections suggests that the new lattice also exhibits a cubic phase. Relatively strong reflections at 2.1 Å can be directly observed in the power spectrum. Figure 4C presents a magnified region indicated by the box in Figure 4A, with the

phase inverted. The lattice structure, where the bright regions represent the projection of clusters of atoms, is visible.

To further elucidate the origin of the supercell, we compare simulated images, generated based on atomic models, with experimental images. The atomic models of the pristine cubic lattice and the supercell with doubled unit cell dimensions are presented in Figures 5A and 5B. In the supercell, the cubic phase is tiled 2x2 in-plane, which results in 12 Na sites, each exhibiting a nominal occupancy of 2/3 in the pristine cubic phase. Then, Na sites are removed from four central positions, adjusting the occupancy of the remaining Na sites from 2/3 to 1. The red dashed and green boxes indicate the dimensions of the unit cell and supercell. The pristine cubic lattice is resolved from the X-ray diffraction,[12, 32, 33] while the supercell model is constructed to assist in determining the potential lattice configuration obtained from the cryo-TEM image. The yellow circle represents vacancies of Na atoms, while the blue circle depicts clusters without vacancies and boron atoms are located at the corner of the box. The simulated diffraction pattern of the supercell model is shown in Figure 5C. Both (100) and (001) reflections exhibit a spacing of 9.4 Å, in contrast to those in the pristine cubic lattice at 4.7 Å (Figure 1B). Potential projections were obtained by applying the multislice method to atomic models using abTEM.[38] The potential projection of supercells is displayed in Figure 5D. The absence of sodium columns due to vacancies results in hollow regions in the lattice, which leads to the formation of a supercell with doubled unit cell dimensions. A simulated bright-field TEM image obtained from a 170.4 Å thick lattice, which is obtained by applying the contrast transfer function used to obtain the experimental image (Figure S5), is presented in Figure 5E. Due to a lack of crystal thickness information in the experimental images, a series of thickness, from 18.8 Å to 300.8 Å

was used for image simulations (Figure S6). The column of boron atoms, the vacancies of Na atoms, and the cluster without Na vacancies are clearly visible compared to the potential projection. The presence of asymmetric clusters and boron atoms are attributed to the absence of correction for high order astigmatisms and axial coma. Figure 5F displays the experimental image obtained by averaging the unit cells in the crystal (see the SI and Figures S7 and S8 for details). The large clusters observed in the experimental image are formed by superposing the sodium ions that occupy the face-centered sites with the NH_2^- cluster anions at the center. The corner bright spots are NH_2^- cluster anions that occupy the corner sites where the adjacent six sodium ions are missing. The presence of vacancies is evident in both the experimental image, where they appear as black regions, and in the simulated image. Compared to the simulated image, the spatial resolution of the experimental image is insufficient to reveal individual atoms within the clusters due to limitations in electron dose, instrument aberrations, and the spatial envelope function. We generated different supercell structures by altering the vacancy ordering and randomly rotating the NH_2 and BH_4 clusters. Thus far, the supercell model depicted in Figure 5B demonstrates the best agreement with the simulated image.

We posit that the superlattice exhibiting vacancy ordering appears during the rapid cooling step. However, since the cooling rate was not measured, it remains uncertain whether the rate was sufficiently fast to immobilize cation migration in the pristine cubic phase. This superlattice may represent a metastable state connecting the phase transition from the cubic to the orthorhombic phase. Further research is needed to determine the extent to which the superlattice is a global structure, as it was not resolved by crystallography. Despite these limitations, cryo-TEM imaging provides invaluable new information about the structural

complexity induced by vacancy ordering in $Na_2NH_2BH_4$ that was not previously observable. It also exhibits the potential for directly imaging the lattices in other antiperovskite-type solid electrolytes, whose structural determinations have been limited to the use of X-ray diffraction.

A reliable cryogenic transfer protocol, which utilizes reusable containers and close contact with cryogen, was used to transfer air-sensitive antiperovskite crystal $Na_2NH_2BH_4$ for cryo-TEM imaging without notable exposure to air. The critical dose was measured to assess the extent of radiation damage at both cryogenic and room temperatures. Remarkably, cryogenic temperatures provided a six-fold improvement in beam stability for this solid electrolyte. Cryo-TEM images obtained from flat crystals revealed the presence of a long-range-ordered supercell with a cubic phase. Notably, this supercell exhibited doubled unit cell dimensions, measuring 9.4 Å x 9.4 Å, in contrast to the cubic lattice structure previously determined by X-ray crystallography, which measured 4.7 Å x 4.7 Å. The absence of 9.4 Å spacing in the diffraction patterns and X-ray crystallography obtained from bulk suggests that only the flat crystals exhibit the superlattice due to the vacancy ordering during cooling. In addition, the presence of these flat crystals, which appear as a minor component in the electrolyte pellet, is a notable discovery that has not been previously identified. Comparisons between the atomic models, simulated images, and experimental images shed light on the origin of this supercell, attributing it to the vacancy ordering of sodium atoms. The cryo-TEM imaging in position space revealed previously unobserved structural complexities not apparent through X-ray diffraction. This study demonstrates a successful strategy for preserving and imaging the highly ordered lattice structures of $Na_2NH_2BH_4$ antiperovskite-type solid electrolytes despite the combined challenges in these materials of high air and beam sensitivity.

Supporting Information:

Experimental section, including sample preparation, EDS, electron diffraction, cryo-TEM data collection and processing, a supplementary movie S1, and supplementary figures from S1 to S8. Two CIF files for the pristine cubic lattice and the proposed super lattice.

Acknowledgments:

Primary funding for this work was provided by the Joint Center for Energy Storage Research (JCESR), an Energy Innovation Hub funded by Office of Science, and Basic Energy Sciences, U.S. Department of Energy. Cryo-TEM data collection and processing at the Donner Cryo-EM resources in Lawrence Berkeley National Laboratory was supported by the Soft Matter Electron Microscopy Program (KC11BN), supported by the Office of Science, Office of Basic Energy Science, US Department of Energy, under Contract DE-AC02-05CH11231. Work at the Molecular Foundry was supported by the Office of Science, Office of Basic Energy Sciences, of the U.S. Department of Energy under Contract No. DE-AC02-05CH11231. The authors acknowledge discussions with Prof. Nitash P. Balsara, Dr. Stephanie M. Ribet at Lawrence Berkeley National Laboratory, and Prof. James M. LeBeau at Massachusetts Institute of Technology.

Author contributions:

Blanka E. Janicek (B.E.J) and Xi Jiang (X.J) designed research. Sunil Mair (S.M) and Yet-Ming Chiang (Y.M.C) synthesized antiperovskite crystals. B.E.J carried out sample preparation, EDS, electron diffraction and cryo-TEM imaging and analysis. Colin Ophus (C.O) wrote the scripts for

cryo-TEM image analysis and processing. X. J wrote the manuscript. All authors contributed to the revision of the manuscript.

Conflict of Interest Statement:

The authors declare no competing financial interest.

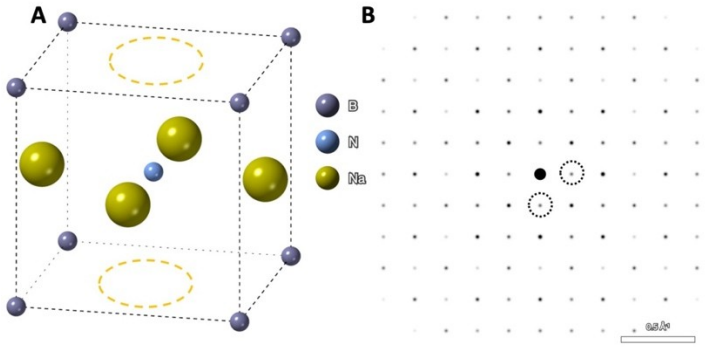

Figure 1. A. The schematic crystal structure of $Na_2NH_2BH_4$. Vacancies are indicated by dashed circles. Hydrogen atoms are omitted for clarity. **B.** Simulated electron diffraction pattern of the $Na_2NH_2BH_4$ with the cubic lattice. The two dashed circles represent the [100] and [010] spots at 4.7 Å, respectively.

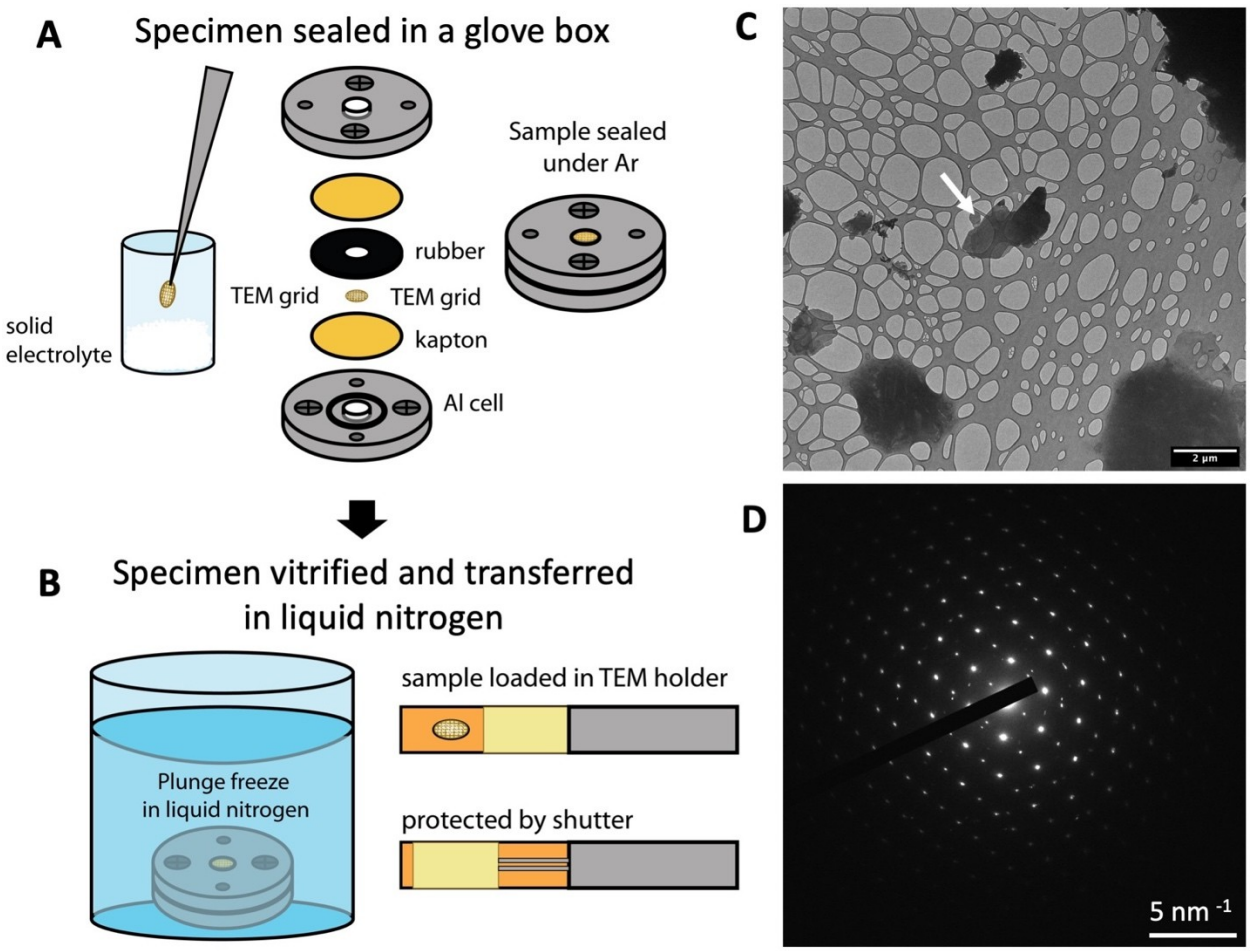

Figure 2. The cryogenic preservation and transfer of $Na_2NH_2BH_4$ crystals. **A.** A TEM grid with crystals is sealed in a container in the glove box. **B.** The container is moved out of the glovebox and plunged into liquid nitrogen to freeze the crystal. The grid was removed from the container and transferred to a TEM cryo-transfer holder under liquid nitrogen. **C.** A TEM micrograph shows the morphology of cryo-transferred crystals. **D.** An electron diffraction pattern obtained from the crystal indicated by the arrow in **C**.

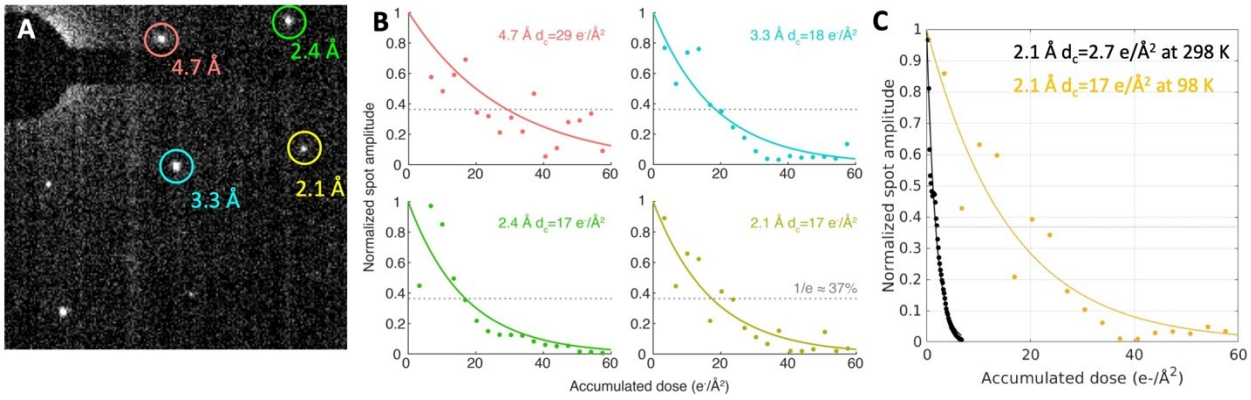

Figure 3. The measurement of critical dose. **A.** A section of a selected area electron diffraction pattern obtained from a $Na_2NH_2BH_4$ crystal at cryogenic temperature. Four reflections at different spatial frequencies are labeled by circles for quantitative measurements of critical dose. **B**. Critical dose measurements of the indicated reflections in A at 4.7 Å (red), 3.3 Å (blue), 2.4 Å (green) and 2.1 Å (yellow), respectively. **C**. The comparison of the critical dose at 2.1 Å at room temperature (black) and the cryogenic temperature (yellow). A six-fold improvement in critical dose is observed.

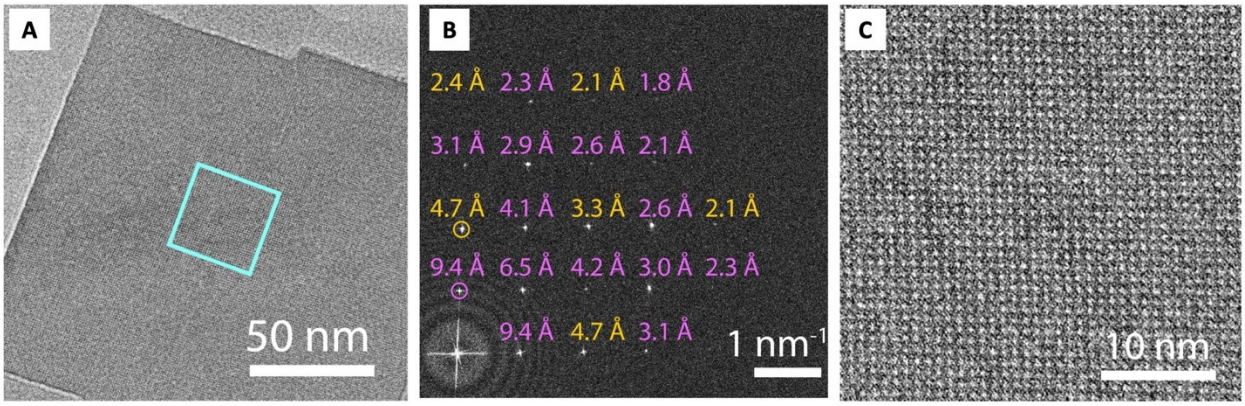

Figure 4. High-resolution cryo-TEM images of Na2NH2BH4 crystals. **A**. A CTF-corrected low-dose micrograph shows a flat crystal with sharp edges. The accumulated dose in this micrograph is 22 e/Å^2. **B**. The power spectrum of the micrograph in A. The spatial frequencies of spots are shown in two colors. All spots are observed in the experimental power spectrum, while only the yellow spots are observed from the simulated diffraction pattern in Figure 1. **C**. A magnified area is indicated by the blue box in A. The bright dots represent the electron-dense atoms in the crystal.

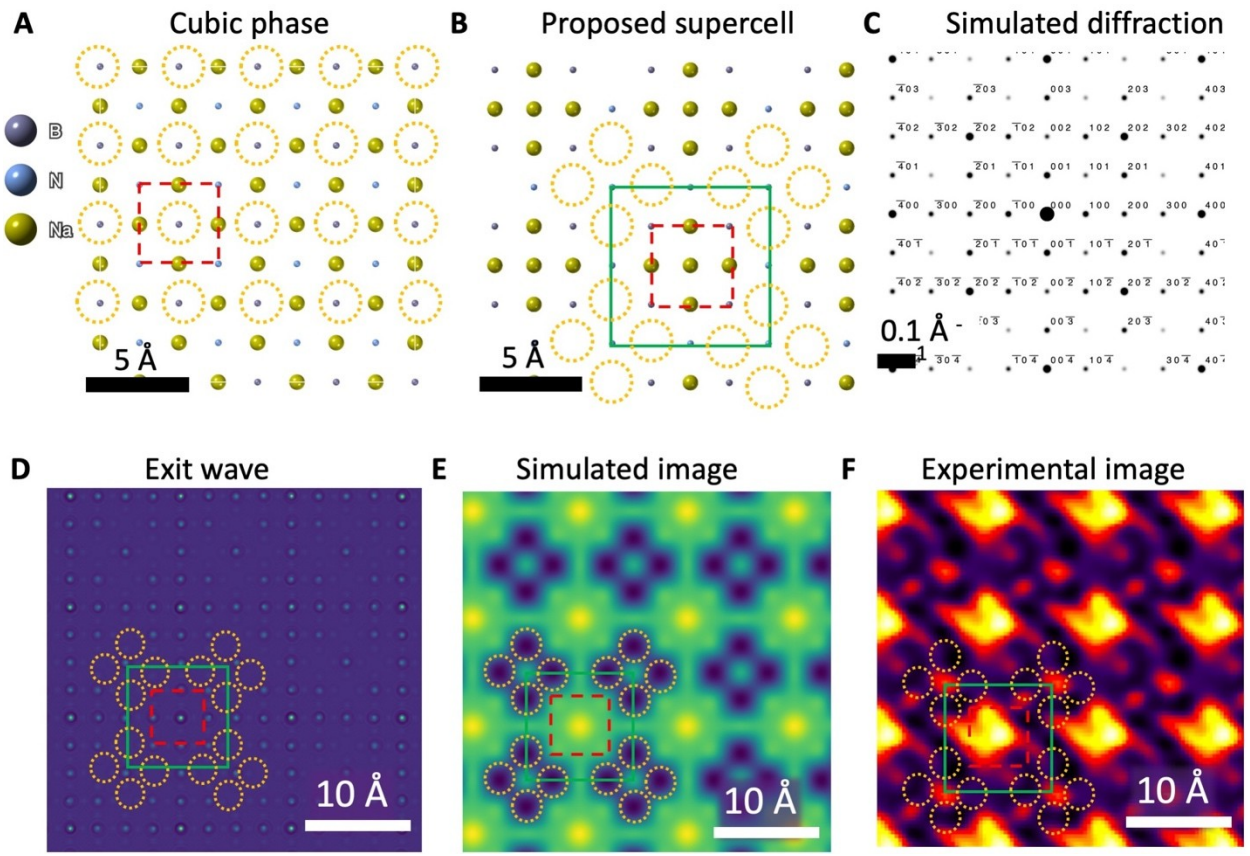

Figure 5. A. The atomic model of the cubic phase, as viewed along the (100) direction. Two of the six sodium ions in a unit cell are missing, as indicated by the yellow circle. BH_4 cluster anions occupy the corner sites, while an NH_2^- anion is located at the center of the unit cell (red dashed box). **B**. The atomic model of a proposed supercell lattice, viewed along the (100) direction, where sodium ions occupy the face-centered sites. NH_2^- cluster anions occupy the corner sites, where adjacent six sodium ions are missing in a unit cell (green box), resulting in doubled dimensions. **C**. The simulated electron diffraction pattern obtained from the atomic model in B. The first-order Bragg spots represent the cubic phase with a spacing of 9.4 Å. **D**. The exit wave image of atoms in B (more unit cells are included for clarity). **E**. A CTF-corrected simulated image based on an atomic model with the thickness of 170.4 Å. **F**. An averaged cryo-TEM image showing the clusters in the flat crystal.

References:

1. A. Kim, S. Woo, M. Kang, H. Park and B. Kang: Research Progresses of Garnet-Type Solid Electrolytes for Developing All-Solid-State Li Batteries *Front Chem.* **8**, 468 (2020).
2. Y. Lee, J. Jeong, H.J. Lee, M. Kim, D. Han, H. Kim, J.M. Yuk, K.W. Nam, K.Y. Chung, H.G. Jung and S. Yu: Lithium Argyrodite Sulfide Electrolytes with High Ionic Conductivity and Air Stability for All-Solid-State Li-Ion Batteries *Acs Energy Letters.* **7**(1), 171 (2022).
3. S. Stramare, V. Thangadurai and W. Weppner: Lithium lanthanum titanates: A review *Chemistry of Materials.* **15**(21), 3974 (2003).
4. J.C. Bachman, S. Muy, A. Grimaud, H.H. Chang, N. Pour, S.F. Lux, O. Paschos, F. Maglia, S. Lupart, P. Lamp, L. Giordano and Y. Shao-Horn: Inorganic Solid-State Electrolytes for Lithium Batteries: Mechanisms and Properties Governing Ion Conduction *Chemical Reviews.* **116**(1), 140 (2016).
5. Q. Liu, X.H. Zhao, Q. Yang, L.J. Hou, D.B. Mu, G.Q. Tan, L. Li, R.J. Chen and F. Wu: The Progress in the Electrolytes for Solid State Sodium-Ion Battery *Adv Mater Technol-Us.* **8** 7), 2200822 (2023).
6. P.A. Chater, P.A. Anderson, J.W. Prendergast, A. Walton, V.S.J. Mann, D. Book, W.I.F. David, S.R. Johnson and P.P. Edwards: Synthesis and characterization of amide-borohydrides: New complex light hydrides for potential hydrogen storage *Journal of Alloys and Compounds.* **446**, 350 (2007).
7. L. Karlsson and R.L. Mcgreevy: Mechanisms of Ionic-Conduction in Li2so4 and Linaso4 - Paddle Wheel or Percolation *Solid State Ionics.* **76**(3-4), 301 (1995).
8. D. Wilmer, K. Funke, M. Witschas, R.D. Banhatti, M. Jansen, G. Korus, J. Fitter and R.E. Lechner: Anion reorientation in an ion conducting plastic crystal - coherent quasielastic neutron scattering from sodium ortho-phosphate *Physica B.* **266**(1-2), 60 (1999).
9. Y.G. Wang, Q.F. Wang, Z.P. Liu, Z.Y. Zhou, S. Li, J.L. Zhu, R.Q. Zou, Y.X. Wang, J.H. Lin and Y.S. Zhao: Structural manipulation approaches towards enhanced sodium ionic conductivity in Na-rich antiperovskites *Journal of Power Sources.* **293**, 735 (2015).
10. Y.L. Sun, Y.C. Wang, X.M. Liang, Y.H. Xia, L.F. Peng, H.H. Jia, H.X. Li, L.F. Bai, J.W. Feng, H. Jiang and J. Xie: Rotational Cluster Anion Enabling Superionic Conductivity in Sodium-Rich Antiperovskite Na3OBH4 *Journal of the American Chemical Society.* **141**(14), 5640 (2019).
11. J.G. Smith and D.J. Siegel: Low-temperature paddlewheel effect in glassy solid electrolytes *Nature Communications.* **11**(1), 1483 (2020).
12. P.C. Tsai, S. Mair, J. Smith, D.M. Halat, P.H. Chien, K. Kim, D.H. Zhang, Y.L. Li, L. Yin, J. Liu, S.H. Lapidus, J.A. Reimer, N.P. Balsara, D.J. Siegel and Y.M. Chiang: Double Paddle-Wheel Enhanced Sodium Ion Conduction in an Antiperovskite Solid Electrolyte *Advanced Energy Materials.* **13**(7), 2203284 (2023).

13. Z.F. Sun, M. Li, B.S. Xiao, X. Liu, H.C. Lin, B. Jiang, H.D. Liu, M.C. Li, D.L. Peng and Q.B. Zhang: In situ transmission electron microscopy for understanding materials and interfaces challenges in all-solid-state lithium batteries *Etransportation.* **14**, 100203 (2022).
14. R.W. Shao, Z.F. Sun, L. Wang, J.H. Pan, L.C. Yi, Y.G. Zhang, J.J. Han, Z.P. Yao, J. Li, Z.H. Wen, S.Q. Chen, S.L. Chou, D.L. Peng and Q.B. Zhang: Resolving the Origins of Superior Cycling Performance of Antimony Anode in Sodium-ion Batteries: A Comparison with Lithium-ion Batteries *Angewandte Chemie-International Edition.* **63**(11), e202320183 (2024).
15. Z.F. Sun, J.H. Pan, W.W. Chen, H.Y. Chen, S.H. Zhou, X.Y. Wu, Y.S. Wang, K. Kim, J. Li, H.D. Liu, Y.F. Yuan, J.W. Wang, D. Su, D.L. Peng and Q.B. Zhang: Electrochemical Processes and Reactions In Rechargeable Battery Materials Revealed via In Situ Transmission Electron Microscopy *Advanced Energy Materials.* **14**(2), 2303165 (2024).
16. Z. Fan, L.Q. Zhang, D. Baumann, L. Mei, Y.X. Yao, X.D. Duan, Y.M. Shi, J.Y. Huang, Y. Huang and X.O.E. Duan: In Situ Transmission Electron Microscopy for Energy Materials and Devices *Advanced Materials.* **31**(33), 1900608 (2019).
17. Y.Y. Zhou, H. Sternlicht and N.P. Padture: Transmission Electron Microscopy of Halide Perovskite Materials and Devices *Joule.* **3**(3), 641 (2019).
18. Y.B. Li, W. Huang, Y.Z. Li, W. Chiu and Y. Cui: Opportunities for Cryogenic Electron Microscopy in Materials Science and Nanoscience *Acs Nano.* **14**(8), 9263 (2020).
19. K.P. Song, L.M. Liu, D.L. Zhang, M.P. Hautzinger, S. Jin and Y. Han: Atomic-Resolution Imaging of Halide Perovskites Using Electron Microscopy *Advanced Energy Materials.* **10**(26), 1904006 (2020).
20. Z.W. Zhang, Y. Cui, R. Vila, Y.B. Li, W.B. Zhang, W.J. Zhou and W. Chiu: Cryogenic Electron Microscopy for Energy Materials *Accounts of Chemical Research.* **54**(18), 3505 (2021).
21. R.F. Egerton: Radiation damage to organic and inorganic specimens in the TEM *Micron.* **119**, 72 (2019).
22. M.J. Zachman, Z.Z. Yang, Y.G. Du and M.F. Chi: Robust Atomic-Resolution Imaging of Lithium in Battery Materials by Center-of-Mass Scanning Transmission Electron Microscopy *Acs Nano.* **16**(1), 1358 (2022).
23. C.Q. Yang, R. Zhi, M.U. Rothmann, Y.Y. Xu, L.Q. Li, Z.Y. Hu, S.P. Pang, Y.B. Cheng, G. Van Tendeloo and W. Li: Unveiling the Intrinsic Structure and Intragrain Defects of Organic-Inorganic Hybrid Perovskites by Ultralow Dose Transmission Electron Microscopy *Advanced Materials.* 35 (17), 2211207 (2023).
24. Y.Z. Li, Y.B. Li, A.L. Pei, K. Yan, Y.M. Sun, C.L. Wu, L.M. Joubert, R. Chin, A.L. Koh, Y. Yu, J. Perrino, B. Butz, S. Chu and Y. Cui: Atomic structure of sensitive battery materials and Interfaces revealed by cryo-electron microscopy *Science.* **358**(6362), 506 (2017).

25. M.J. Zachman, Z.Y. Tu, S. Choudhury, L.A. Archer and L.F. Kourkoutis: Cryo-STEM mapping of solid-liquid interfaces and dendrites in lithium-metal batteries *Nature.* **560**(7718), 345 (2018).
26. E. Zhang, M. Mecklenburg, X.T. Yuan, C.Z. Wang, B. Liu and Y.Z. Li: Expanding the cryogenic electron microscopy toolbox to reveal diverse classes of battery solid electrolyte interphase *Iscience.* **25**(12), 105689 (2022).
27. Z.W. Zhang, Y.Z. Li, R. Xu, W.J. Zhou, Y.B. Li, S.T. Oyakhire, Y.C. Wu, J.W. Xu, H.S. Wang, Z.A. Yu, D.T. Boyle, W. Huang, Y.S. Ye, H. Chen, J.Y. Wan, Z.N. Bao, W. Chiu and Y. Cui: Capturing the swelling of solid-electrolyte interphase in lithium metal batteries *Science.* **375**(6576), 66 (2022).
28. C.M. Wang: In situ transmission electron microscopy and spectroscopy studies of rechargeable batteries under dynamic operating conditions: A retrospective and perspective view *Journal of Materials Research.* **30**(3), 326 (2015).
29. Y.B. Xu, H.P. Wu, H. Jia, M.H. Engelhard, J.G. Zhang, W. Xu and C.M. Wang: Sweeping potential regulated structural and chemical evolution of solid-electrolyte interphase on Cu and Li as revealed by cryo-TEM *Nano Energy.* **76**, 105040 (2020).
30. Y.B. Xu, H.P. Wu, H. Jia, J.G. Zhang, W. Xu and C.M. Wang: Current Density Regulated Atomic to Nanoscale Process on Li Deposition and Solid Electrolyte Interphase Revealed by Cryogenic Transmission Electron Microscopy *Acs Nano.* **14**(7), 8766 (2020).
31. X.F. Wang, Y.J. Li and Y.S. Meng: Cryogenic Electron Microscopy for Characterizing and Diagnosing Batteries *Joule.* **2**(11), 2225 (2018).
32. M. Somer, S. Acar, C. Koz, I. Kokal, P. Höhn, R. Cardoso-Gil, U. Aydemir and L. Akselrud: α- and β-Na[BH][NH]: Two modifications of a complex hydride in the system NaNH-NaBH; syntheses, crystal structures, thermal analyses, mass and vibrational spectra *Journal of Alloys and Compounds.* **491**(1-2), 98 (2010).
33. M. Matsuo, S. Kuromoto, T. Sato, H. Oguchi, H. Takamura and S. Orimo: Sodium ionic conduction in complex hydrides with [BH4](-) and [NH2](-) anions *Applied Physics Letters.* **100**(20), 203904 (2012).
34. J. Quinn, B.B. Wu, Y.B. Xu, M.H. Engelhard, J. Xiao and C.M. Wang: Tracking the Oxidation of Silicon Anodes Using Cryo-EELS upon Battery Cycling *Acs Nano.* **16**(12), 21063 (2022).
35. R.F. Egerton, P. Li and M. Malac: Radiation damage in the TEM and SEM *Micron.* **35**(6), 399 (2004).
36. R.M. Glaeser: Limitations to Significant Information in Biological Electron Microscopy as a Result of Radiation Damage *Journal of Ultrastructure Research.* **36**(3-4), 466 (1971).
37. S. Kumar and W.W. Adams: Electron-Beam Damage in High-Temperature Polymers *Polymer.* **31**(1), 15 (1990).
38. J. Madsen and T. Susi: The abTEM code: transmission electron microscopy from first principles *Open Research Europe.* **1**(24), (2021).

Table of Content